ADVANCES IN ATMOSPHERIC SCIENCES, VOL. 26, NO. 5, 2009, 1015–1026

Simulating Tropical Instability Waves in the Equatorial Eastern Pacific with a Coupled General Circulation Model

CHEN Xianyan*[1] (陈鲜艳) and Masahide KIMOTO[2]

[1] *National Climate Center, China Meteorological Administration, Beijing,* 100081

[2] *Center for Climate System Research, University of Tokyo,* 5-1-5*, Kashiwano-ha, Kashiwa, Japan*

(Received 19 May 2008; revised 19 November 2008)

ABSTRACT

Satellite observations of SSTs have revealed the existence of unstable waves in the equatorial eastern Pacific and Atlantic oceans. These waves have a 20–40-day periodicity with westward phase speeds of 0.4–0.6 m s^{-1} and wavelengths of 1000–2000 km during boreal summer and fall. They are generally called tropical instability waves (TIWs). This study investigates TIWs simulated by a high-resolution coupled atmosphere-ocean general circulation model (AOGCM). The horizontal resolution of the model is 120 km in the atmosphere, and 30 km longitude by 20 km latitude in the ocean. Model simulations show good agreement with the observed main features associated with TIWs. The results of energetics analysis reveal that barotropic energy conversion is responsible for providing the main energy source for TIWs by extracting energy from the meridional shear of the climatological-mean equatorial currents in the mixed layer. This deeper and northward-extended wave activity appears to gain its energy through baroclinic conversion via buoyancy work, which further contributes to the asymmetric distribution of TIWs.

It is estimated that the strong cooling effect induced by equatorial upwelling is partially (∼30%–40%) offset by the equatorward heat flux due to TIWs in the eastern tropical Pacific during the seasons when TIWs are active. The atmospheric mixed layer just above the sea surface responds to the waves with enhanced or reduced vertical mixing. Furthermore, the changes in turbulent mixing feed back to sea surface evaporation, favoring the westward propagation of TIWs. The atmosphere to the south of the Equator also responds to TIWs in a similar way, although TIWs are much weaker south of the Equator.

Key words: tropical instability waves, equatorial eastern Pacific, coupled general circulation model, heat flux, air-sea interaction

Citation: Chen, X. Y., and M. Kimoto, 2009: Simulating tropical instability waves in the equatorial eastern Pacific with a coupled general circulation model. *Adv. Atmos. Sci.*, **26**(5), 1015–1026, doi: 10.1007/s00376-009-8078-7.

1. Introduction

Cusp-shaped tropical instability waves (TIWs) were first noticed in current-meter records in the Atlantic Ocean (Duing et al., 1975) and in thermal infrared images of SSTs in the Pacific Ocean (Legeckis, 1977). These westward-propagating waves were then observed by satellites in sea-level anomalies, sea-surface heights, and surface chlorophyll just north of the Equator in both the eastern tropical Pacific and Atlantic oceans. The waves propagate westward with wavelengths of 1000–2000 km, periods of 20–40 days, and phase speeds of 0.4–0.6 m s^{-1} (Legeckis, 1977; Contreras, 2002).

TIWs are considered to originate in the ocean, but researchers have not yet reached consensus on their generation mechanism. Based on a simple 1.5-layer model, Philander (1976, 1978) hypothesized that TIWs are due to barotropic shear between the South Equatorial Current (SEC) and the North Equatorial Countercurrent (NECC). Cox (1980), using a multilevel ocean model forced by long-term averaged monthly varying winds, confirmed a barotropic generation mechanism via horizontal shearing between the

*Corresponding author: CHEN Xianyan, chenxy@cma.gov.cn

mean flows suggested by Philander and also reported a secondary energy source arising from the vertically sheared current and associated energy conversion from the mean potential energy. A primitive equation model simulation performed by Semtner and Holland (1980) suggested that the major source of the wave energy might be available potential energy. On the other hand, Hansen and Paul (1984) obtained some observational evidence of barotropic and baroclinic instability in their analysis of satellite-traced drifting buoys in the eastern equatorial Pacific Ocean and suggested that both barotropic and baroclinic conversions were of the same magnitude. However, in the Hawaii-to-Tahiti Shuttle Experiment, Luther and Johnson (1990) found that the instability waves were associated with three separate energy sources. One was the barotropic energy conversion arising from current shear between the SEC and the Equatorial Undercurrent (EUC) in boreal summer and fall, just north of the Equator. The other two sources were baroclinic instabilities, manifested by large mean-to-eddy potential energy conversion occurring on the equatorial front at 3°N to 6°N, and by a strong northward eddy heat flux and associated potential energy conversion between 5°N and 9°N. McCreary and Yu (1992) and Yu et al. (1995) suggested that the equatorial temperature front north of the Equator, as well as barotropic instability, were the most important energy sources in their linearized 1.5-layer ocean model. Proehl (1996) proposed that the instability might be a mixture of baroclinic, barotropic, and Kelvin-Helmholtz mechanisms. In their investigation of subsurface mooring data, Qiao and Weisberg (1998) found that the waves were primarily initiated by barotropic instability. However, Masina et al. (1999) and Masina and Philander (1999) investigated the instability mechanism by using an ocean general circulation model, which indicated that the waves developed preferentially in the eastern Pacific along the northern temperature front. They suggested that baroclinic instability is the primary source generating TIWs and pointed out that the energy source is different in different latitudes.

Arguments based on equatorial observations and experimental studies of TIWs energetics have not reached agreement with regard to the primary energy source of TIWs. Although many ocean experiments have been carried out, most available observational data are limited to sparse *in-situ* measurements at specific locations, particularly around the Equator. Numerical models are capable of generating waves with varying basic wave features, such as wavelength and period. However, most previous studies have been based on linearized models; few have used a high-resolution ocean general circulation model (OGCM) or atmosphere-ocean generational circulation model (AOGCM).

TIWs have attracted increased research interest because of two important roles that they may play in the tropical climate. One is the modulation of the heat budget of the ocean mixed layer. Based on satellite-tracked drifting-buoy data, Hansen and Paul (1984) and Swenson and Hansen (1999) suggested that the most active processes for the annual heat cycle of the cold tongue region were mean meridional advection and upwelling. However, the eddy heat transport associated with TIWs acts as a negative feedback that offsets a considerable fraction of the heat transported by the meridional advection and equatorial upwelling due to Ekman divergence of the mean flows in near-surface waters. Yet, again due to sparse data sampling, estimates of equatorward heat flux associated with TIWs have been based primarily on data from a limited number of drifting buoys. Thus, spatially and temporally consistent analysis of a numerical model simulation would be helpful in evaluating the contributions of TIWs to the equatorial oceanic heat budget (Vialard et al., 2003; Jochum et al., 2004).

Furthermore, the eastern tropical Pacific has some of the most vigorous air-sea coupling on the planet; thus the atmospheric adjustment to SST perturbations associated with TIWs should provide us with a new understanding of the coupling between the atmosphere and ocean in the eastern tropical Pacific. Wallace et al. (1989) and Hayes et al. (1989) noticed that surface winds exhibit pronounced horizontal divergence just over the northern branch of the cold tongue as the air flows northward across the oceanic SST front. They introduced a vertical mixing mechanism supposing that vertical stratification decreases when the boundary layer flow passes from cold water to warmer water. As a result, the wind shear near the surface is reduced and thus the surface wind speeds increase. Xie et al. (1998) associated the vertical mixing mechanism with coupling between the surface wind and the wave-induced SST, suggesting that the impact of TIWs on the atmosphere may extend to the planetary boundary layer. Recently, further attempts have been made to investigate the local coupling induced by TIWs over the cold tongue region (Liu et al., 2000; Chelton et al., 2001; Hashizume et al., 2002; Small et al., 2003). However, most of these studies have focused on areas north of the Equator. We have little information on the atmospheric response to TIWs south of the Equator (Chelton et al., 2001). Furthermore, knowledge of the atmospheric feedback to TIWs is also limited. To better describe TIWs activities and associated oceanic and atmospheric responses, comprehensive ocean-atmosphere data generated from realistic

coupled AOGCM simulations may be of great help.

We therefore used a high-resolution global AOGCM to examine the three-dimensional structure of TIWs and the role of these waves in the eastern tropical Pacific climate. We investigated the performance of the model by comparing the results with satellite observations over a complete wave season, from June to December. The results showed that the model was able to well reproduce the main features of TIWs, such as wavelength, period, phase speed, and onset time. We therefore used the simulated data to investigate the energetics of instability waves and to evaluate their contributions to the equatorial ocean heat flux as well as their impact on the atmosphere. This paper is organized as follows. Section 2 briefly describes the model. Section 3 presents the simulated TIWs and their validation against the observations. Section 4 investigates TIWs energetics. The estimated heat flux contribution of TIWs to the eastern tropical Pacific Ocean heat budget and local atmospheric response to TIWs and atmospheric feedback to TIWs are described in sections 5 and 6. The last section presents a summary and discussion.

2. Model

This study uses the Model for Interdisciplinary Research on Climate (MIROC) 3.2, which has been developed cooperatively in Japan by the Center for Climate System Research (CCSR, University of Tokyo), the National Institute for Environmental Studies (NIES), and the Frontier Research Center for Global Change (FRCGC). The model consists of five components: atmosphere, land, river, sea ice, and ocean. A detailed description of the model has been provided by the K-1 Model developers (Hasumi and Emori, 2004). Here the atmosphere and ocean parts of the model are briefly described.

The atmospheric general circulation model used in the MIROC 3.2 coupled AOGCM is the CCSR/NIES/FRCGC atmosphere general circulation model (AGCM) 5.7b (Numaguti et al., 1997). The model is based on primitive equations on a sphere using a spectral transform method for horizontal discretization. The vertical sigma coordinate is employed. The horizontal resolution is a triangular spectral truncation at total wave number 106 (T106), using transform grids of $1.125^\circ \times 1.125^\circ$ longitude by latitude (about 120 km). There are 56 vertical layers in the model with the top at about 40 km. The physical parameterizations include a radiation scheme with a two-stream k-distribution method (Nakajima et al., 2000), a prognostic Arakawa-Schubert cumulus parameterization scheme (Arakawa and Schubert, 1974; Pan and Randall, 1998), a prognostic cloud water scheme for large-scale condensation, a turbulence closure scheme with cloud effects, and an orographic gravity wave drag scheme.

The atmosphere model is coupled with an oceanic component, the CCSR Ocean Component Model (COCO; Hasumi, 2000). Based on primitive equations with the Boussinesq approximation, the domain of COCO is global, with a horizontal resolution of 0.28° longitude (about 30 km) by 0.18° latitude (about 20 km). Vertically, there are 48 levels, including the bottom boundary layer, with 17 levels residing in the upper 200 meters. The vertical diffusion and viscosity coefficients are calculated by the parameterization of Noh and Kim (1999), based on the level-2.5 turbulence closure of Mellor and Yamada (1982).

The ocean and atmosphere are coupled at 3-hour intervals without applying any flux adjustment. All the components of the model have been spun up for more than 100 years.

3. Simulated tropical instability waves

Over the equatorial ocean, southeasterly trade winds prevail across the Equator and feed into ITCZ at around 9°–10°N, converging with northeasterly winds from higher latitudes. The cold tongue on the Equator that extends over the eastern Pacific is associated with the strong tropical equatorial SST front at about 2°N, which separates the cold water to the south from the warm water to the north. TIWs, which appear as cusp-shaped SST undulations, are visible just north of the Equator, as observed by the Tropical Rain Measuring Mission (TRMM) microwave imager (TMI; Hashizume et al., 2001; Chelton et al., 2000). Recent observations have supported the existence of TIWs in the Southern Hemisphere (Contreras, 2002). The model simulation also shows weaker and broader cusp-like undulations to the south of the Equator.

An approximate east-west wavelength of 9°–11°N longitude (about 1000–1200 km) can be identified in the SST ridges and in current vortices, with a slightly longer wavelength in the east and shorter wavelength in the west. Analysis of the simulated power spectra for SSTs in different locations shows that the fluctuations in SST near the Equator have a periodicity of around 25 days. Thus a 10- to 50-day bandpass filter is applied to SSTs to isolate the TIWs signals in the cold tongue area. This reveals about seven wave packets that develop and propagate westward during the wave season (June to December), similar to observational results by Xie et al. (1998). Furthermore, as shown in the power spectra, the TIWs signals are most evident on, and just north of, the Equator. They prop-

agate westward with an almost constant phase speed of approximately 0.6 m s^{-1}, slowing slightly west of 140°W. The onset of the TIWs occurs between the end of May and early July, with the magnitude of temperature anomalies peaking by up to almost 3 degrees during boreal fall. Weak, but still discernible, wave signals also develop in June to the south of the Equator and are most clearly seen between August and November. Overall, the model captures the main features of TIWs, such as their wavelength, phase-speed period, and seasonality.

The fact that TIWs activity at the ocean surface is most pronounced around 2°N in the Pacific Ocean is shown in the spatial distribution of SST, which is consistent with satellite observations. Since TIWs have an oceanic origin, their signals are clearly discernible under the sea surface during the wave season. Figure 1 shows the vertical structure of the TIWs activity along 120°W associated with the meridional displacements by the regression coefficients map of ocean temperature against 10- to 50-day bandpass-filtered SSTs at 2°N, 120°W, where the variability of the bandpassed filtered ocean temperature down to a deeper depth. The maximum of wave variability is near the Equator, confined to the upper ocean within the mixed layer with no significant contribution below 100 m. The near-surface TIWs' signals are found within only 4°N–4°S. Fluctuations in sub-surface temperatures seem to have a broader latitudinal extension, where the TIWs signals in the subsurface are clear up to around 7°N, although at the surface they disappear around 4°N, as shown in Fig. 1. Several observations have been reported, such as subsurface oscillations associated with TIWs in the

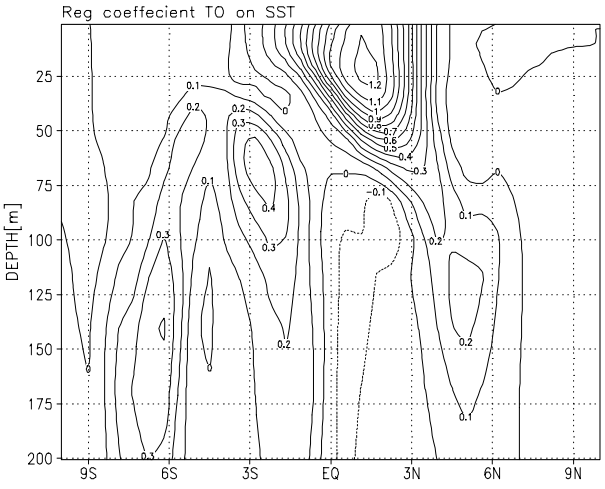

Fig. 1. Regression coefficients of the ocean temperature against 10- to 50-day bandpass-filtered SSTs at 2°N, 120°W. Unit: °C °C^{-1}.

thermocline layer off the Equator (McPhaden et al., 1998; Lyman et al., 2007). However, few numerical simulations have reproduced these fluctuations with such depth or latitude. A possible reason for this is that simplified or coarse-resolution models fail to reproduce the ocean subsurface background that generates TIWs. Since most previous studies have focused on TIWs near the Equator, less is known about the sub-surface component. Thus, a question arises as to which process is responsible for the temperature fluctuations of the deeper layer. Given the good agreement of the model simulation of TIWs, we investigate the energetic source of the simulated waves in the next section and try to determine what instability mechanism may be responsible for generating TIWs in the deeper layer off the Equator.

4. Energetics of the waves

The distribution of eddy kinetic energy represents TIWs activity well. Following Hansen and Paul (1984) and Jochum et al. (2004), we decompose the velocity and temperature fields into mean and fluctuation components:

$$\begin{cases} u = \overline{u} + u' \\ v = \overline{v} + v' \\ T = \overline{T} + T' \,, \end{cases} \tag{1}$$

where the u, v is the velocity of ocean currents and T is the ocean temperature. The overbar denotes the 40-day running mean and the prime denotes deviation thereof. Unless stated otherwise, this eddy definition is used hereafter.

The eddy kinetic energy is then denoted as EKE = $\frac{1}{2}(u'^2 + v'^2)$. Figure 2a shows the annual mean EKE, which is compared with the mean kinetic energy [defined as MKE= $\frac{1}{2}(\bar{u}^2 + \bar{v}^2)$] at 120°W. The maxima of MKE correspond to major ocean currents with a peak located just on the Equator at 100 m depth near the core of the EUC; two secondary maxima are located on either side of the Equator near the surface, corresponding to the two branches of the SEC (Fig. 2b).

A pronounced feature of the annual EKE is an asymmetric distribution with respect to the Equator. The maximum amplitude is found near the surface just north of the Equator. A secondary maximum in EKE is between the EUC and the northern branch of the SEC in the mixed layer. In deeper waters, the EKE penetrates downward and poleward. Below 100-m depth, the EKE is concentrated between 4°N and 6°N, consistent with the fluctuations in TIWs temperatures at that depth. The analysis of the temporal variations of EKE also shows that the EKE averaged

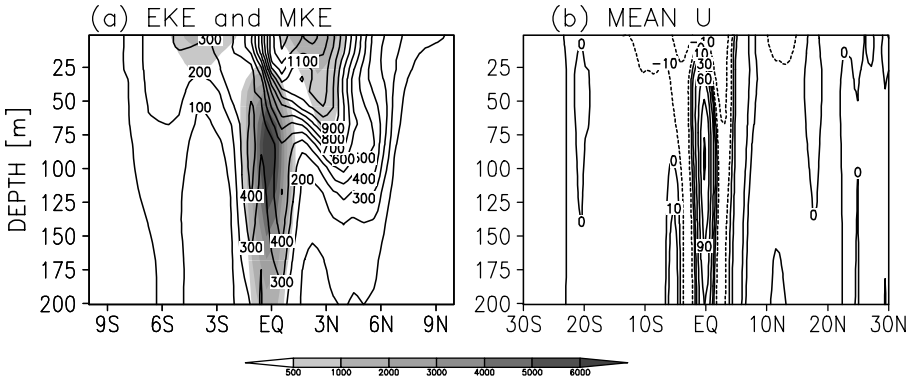

Fig. 2. Depth-latitude plot at 120°W of (a) the annual averages of the mean kinetic energy (shaded, $\mathrm{cm^2\ s^{-2}}$) and eddy kinetic energy (contour, $\mathrm{cm^2\ s^{-2}}$) and (b) mean ocean zonal current ($\mathrm{cm\ s^{-1}}$).

over 0–54 m depths peaks along 2°N during the wave season, indicating that surface-confined TIWs variability is confined to near the Equator. On the other hand, EKE averaged over 99–140 m depths shows that the energy along 4°N remains larger than that along 2°N throughout the wave season. This is consistent with Fig. 1, suggesting the variability in TIWs in deeper waters.

Take U as mean horizontal vector ocean current and u is the zonal velocity of U, w is the vertical velocity of ocean current, ρ is ocean density, ρ_0 is mean ocean density and p is ocean pressure. The eddy kinetic energy budget (EKE) is examined following Eq. (2) below (see Weisberg and Weingartner, 1988 and Qiao and Weisberg, 1998):

$$(\mathrm{EKE})_t + \boldsymbol{U}\cdot\nabla(\mathrm{EKE}) + \boldsymbol{u'}\cdot(\mathrm{EKE}) = \underbrace{-\overline{<\boldsymbol{u'}\cdot\nabla p'>}}_{\text{(a)}} + \underbrace{\rho_0\overline{<\boldsymbol{u'}\cdot(\boldsymbol{u'}\cdot\nabla\boldsymbol{U})>}}_{\text{(b)}} - \underbrace{g\overline{<\rho' w'>}}_{\text{(c)}}\ , \tag{2}$$

where the angle brackets denote a 40-day running mean and the primes are the deviations from the running mean, as before.

The first term (a) on the right-hand side denotes the contribution of pressure work by redistributing eddy energy. The second term (b) is the deformation term, which is the energy conversion between the mean flows and eddies through the Reynolds stress. The last term (c) is the energy conversion between eddy kinetic energy and eddy potential energy through buoyancy work.

Figure 3 shows the vertical distribution of the annually averaged pressure work term. The two distinct negative maxima between the Equator and 3°N show that the pressure work is a sink rather than a source in the main TIWs region. This result is consistent with some previous observational results; for example, Qiao and Weisberg (1998) found that pressure work tends to weaken TIWs by radiating perturbation energy meridionally out of the equatorial region.

The deformation term can be expanded as follows:

$$\begin{aligned}-\rho_0\overline{<\boldsymbol{u'}\cdot(\boldsymbol{u'}\cdot\nabla\boldsymbol{U})>} = &-\rho_0(U_x\overline{<u'u'>} + \\ &U_y\overline{<u'v'>} + V_x\overline{<u'v'>} + \\ &V_y\overline{<v'v'>} + U_z\overline{<u'w'>} + \\ &V_z\overline{<v'w'>})\ .\end{aligned} \tag{3}$$

Figure 4 shows the annual mean of each term on the right-hand side of Eq. (3), averaged between 100°W and 140°W in the uppermost 40 m. The lead term is $-\rho_0 U_y\overline{<u'v'>}$, which represents the energy conversion from the meridional shear of the mean flows by way of the Reynolds stress. Large positive values occur at the Equator and between 3°N and 4°N. The secondary large term is $-\rho_0 V_y\overline{<v'v'>}$, which results from Ekman divergence of the mean flows. However,

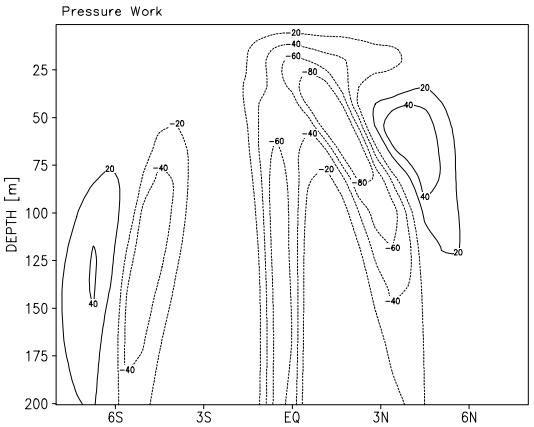

Fig. 3. Depth-latitude cross-section of the annual mean pressure work. Units: $\mathrm{g\ cm^{-1}\ s^{-3}}$.

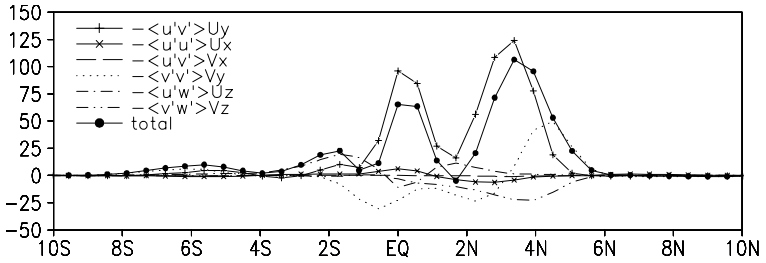

Fig. 4. Annual mean of the deformation term of Eq. 2 (black dotted line) averaged between 100°W and 140°W in the uppermost 40 m of the ocean. Each sub-term of the deformation term is indicated in the panel. Units: g cm^{-1} s^{-3}.

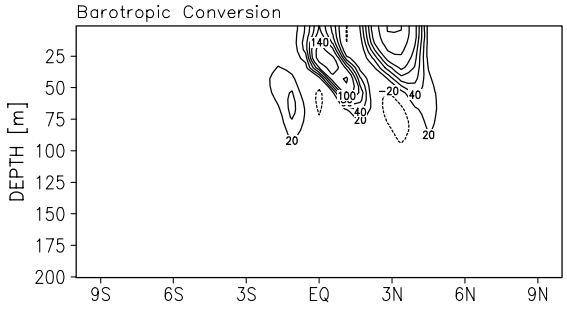

Fig. 5. Latitude-depth cross-section of the annual mean of barotropic conversion, $-\rho_0 U_y \overline{< u'v' >}$, along 120°W. Units: g cm^{-1} s^{-3}.

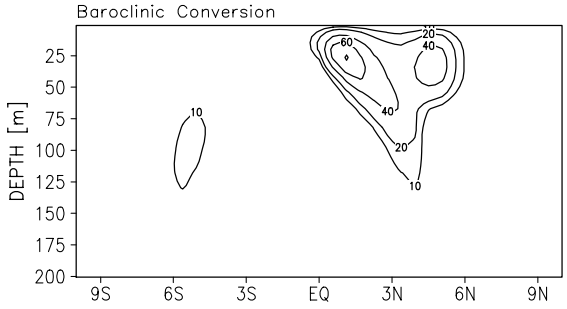

Fig. 6. Latitude-depth cross-section of the annual mean baroclinic conversion, $-g\overline{< \rho'w' >}$, averaged between 120°W and 160°W. Units: g cm^{-1} s^{-3}.

the near-surface contribution of Ekman divergence is negative except in latitudes north of 3°N. Apparently, Ekman divergence generally acts as a sink to eddy kinetic energy (Qiao and Weisberg, 1998). The other terms, though not negligible, are of smaller magnitude. Therefore, the conversion term from the mean meridional shear, $-\rho_0 U_y \overline{< u'v' >}$, is the most important among the deformation terms. This contribution is generally referred to as barotropic energy conversion.

The dominant contribution of barotropic energy conversion to TIWs energetics has been suggested by Qiao and Weisberg (1998). Based on current velocity data from the Tropical Instability Wave Experiment (TIWE) array and temperature data from the Tropical Ocean Global Atmosphere Tropical Atmosphere Ocean (TOGA TAO) array, they pointed out that the value of 100 g cm^{-1} s^{-3} of barotropic energy conversion was large enough to support the initial wave growth. They also reported observed fluctuations in this energy source during the TIWE observation experiments. However, due to the sparseness of data, the energetics analysis of Qiao and Weisberg (1998) was limited to the near-equatorial region. Thus, their barotropic energy conversion was mainly concerned with the cyclonic shear between the SEC and EUC near the Equator. Figure 5 shows the latitude-depth cross-section of the annually averaged barotropic conversion, $-\rho_0 U_y \overline{< u'v' >}$, along 120°W. Two large positive values can be seen north of the Equator. One is located between the boundary of the SEC and EUC, and the other is near the sea surface around 3–4°N. Therefore, the anti-cyclonic shear between the SEC and the NECC may also be a potential energy source for TIWs. Observational evidence supporting this suggestion has been found by Flament et al. (1996). They conducted extensive measurements by shipboard sensors and drifting buoys centered near 3.417°N, 140°W in 1990 and found that fluctuations in TIWs near 3.417°N, 140°W arose mostly from shear between the SEC and NECC. In this way, the model simulation suggests that both the cyclonic shear between the SEC and EUC near the Equator and the anti-cyclonic shear between the SEC and NECC are potential sources for TIWs, as shown in Fig. 5. A positive maximum in depth is also shown south of the Equator, which contributes to TIWs in the subsurface layer.

Figure 5 shows that the distribution of the barotropic conversion term is generally confined to the upper 100 m. While explaining the generation of TIW variability in the upper ocean, it fails to explain the variability of TIWs penetrating into the subsurface layer. In Fig. 6, where the depth-latitude cross-section

of the last term, $g\overline{<\rho' w'>}$, usually called baroclinic energy conversion, is shown. In contrast to the barotropic conversion, positive values slope downward and poleward. The magnitude of baroclinic energy conversion in deeper depths contributes to the wave variability in the sub-surface layer.

The possible contribution of baroclinic conversion to TIWs has been reported in previous studies. For instance, Cox (1980), using a multilevel numerical model, indicated that the energy from the buoyancy terms fed the simulated waves. In a recent ocean GCM numerical estimation of TIWs energetics in the equatorial Pacific, Masina et al. (1999) and Masina and Philander (1999) also suggested that baroclinic instability is the major source for eddies. However, Cox's baroclinic conversion estimation was based on an area and depth average, and Masina's model failed to obtain the SEC-NECC shear. Luther and Johnson (1990) reported observational evidence of baroclinic energy for generating TIWs, suggesting that TIWs eddies might obtain baroclinic energy in the northern equatorial cold tongue temperature front region. Moreover, Qiao and Weisberg (1998) also suggested that within 1°N–1°S the baroclinic conversion through buoyancy work would be small and even negative. The present model simulation is in good agreement with these observations (Fig. 6).

Thus, in summary, the MIROC 3.2 simulation suggests that both barotropic and baroclinic energy conversion is responsible for the generation of TIWs. The surface-trapped barotropic conversion at and just north of the Equator is the main source of eddies during the season of TIWs. However, baroclinic energy conversion is important as well. Although its magnitude is smaller than the barotropic conversion (about 1/3 of the barotropic energy conversion; Fig. 5 and Fig. 6), the poleward slope of the baroclinic conversion explains the temperature fluctuations below the mixed layer, contributing to the asymmetric structure of TIWs.

5. Impact of TIWs on oceanic climate

The surface waters of the equatorial eastern Pacific are cooled by equatorial upwelling. However, when TIWs develop, the associated eddy meridional heat flux, $\overline{<v'T'>}$, is negative north of the Equator and positive south of the Equator (Fig. 7), indicating an equatorward eddy heat flux in the near-surface waters of both hemispheres. Figure 8 shows the horizontal distribution of the eddy heat flux convergence and divergence during the wave season, averaged between the surface and the 100 m depth. A clear band of convergence (positive value shown in Fig. 8) is located near the Equator. The numerical simulation shows that the wave-season mean of the eddy heat flux convergence is about 71 W m^{-2}, while the convergence of climatological upwelling, mainly from Ekman divergence, is approximately -187 W m^{-2} for the annual mean and -224 W m^{-2} for the wave-season mean. Although the magnitude of the eddy heat flux convergence is smaller than that of the climatological upwelling, the equatorward heat transport by TIWs may be of potential importance for the equatorial ocean heat budget by offsetting approximately 30%–40% of the cooling effect from the mean flows (Fig. 9). This simulation result is consistent with the observational estimations of TIWs heat flux by Hansen and Paul (1984) and Swenson and Hansen (1999) for the Pacific Ocean. Swenson and Hansen (1999) obtained an eddy heat flux convergence magnitude of around 42 W m^{-2} for an annual mean and 180 W m^{-2} for a weekly mean near the Equator. This result is also consistent with the estimation by Weisberg and Weingartner (1988) for the Atlantic Ocean; they suggested a surface flux of about 100 W m^{-2} from TIWs averaged over the wave season.

The present simulation results are encouraging. First, they show that the waves make a significant con-

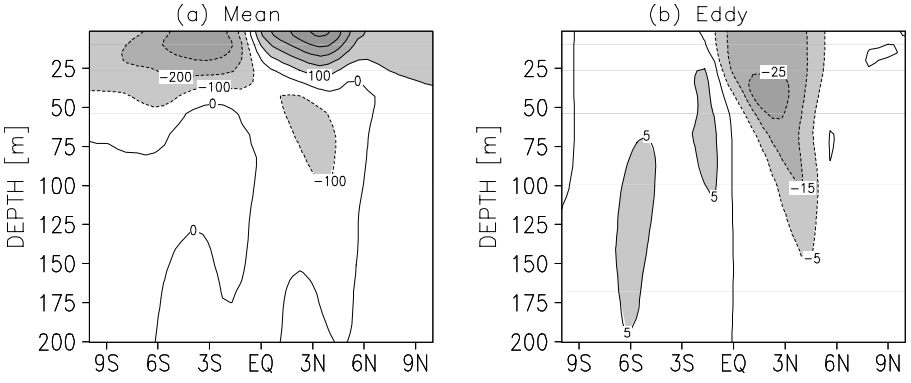

Fig. 7. The mean meridional heat flux $\overline{<\overline{v}\overline{T}>}$ and eddy meridional heat flux $\overline{<v'T'>}$ averaged between 140°W and 120°W. Units: K cm s^{-1}.

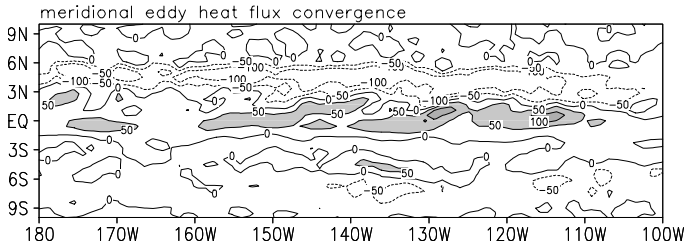

Fig. 8. Meridional eddy heat flux convergence (positive) and divergence (negative) integrated between the surface and 100 m during the tropical instability waves (TIWs) season (1 June–1 December in model year 0018). Units: W m^{-2}.

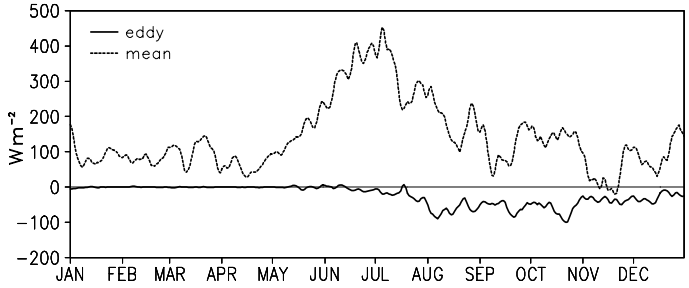

Fig. 9. Time series of the mean meridional heat flux divergence and eddy meridional heat flux divergence averaged over the region of 2°N–2°S, 140°–120°W. Units: W m^{-2}.

tribution to the heat budget in the equatorial ocean by moderating the cooling trend from the mean flows. Furthermore, the eddy meridional heat flux itself would yield a SST heating rate of around 3×10^{-7} °C s^{-1}. The values for the eddy horizontal and vertical temperature flux are 0.1×10^{-7} °C s^{-1} and -1.7×10^{-7} °C s^{-1}, respectively. Hence, a net eddy temperature flux of about 1.4×10^{-7} °C s^{-1} provides an overall warming effect in the cold tongue area, which would increase the equatorial SST by 2°C during the wave season. Incorporation of TIWs may improve the tropical climate simulations of the general circulation models, since the cold tongue in the tropical Pacific tends to extend too far west and have a cold bias in most current OGCM and AOGCM simulations. Better tropical climate simulation would thus be expected in terms of the waves' potential to reduce the cold bias of the equatorial SSTs between the numerical model simulations and observations, through heat transport into the equatorial cold tongue.

6. Atmospheric response and feedback to TIWs

Figure 10 illustrates the effect of TIWs SST variation on the atmosphere. An undulating band of wind stress divergence is collocated with the cusp-shaped SST front just north of the Equator. Such a relationship between the wind stress and SST was assumed to be a vertical mixing mechanism by Wallace et al. (1989) and Hayes et al. (1989). That is, over the cold tongue the air is stably stratified when it crosses the northern boundary of the equatorial cold tongue toward the warm waters; the atmospheric boundary layer then undergoes a transition from a stable to an unstable regime, favoring an increase in surface wind speed through the buoyant turbulence, which results in pronounced horizontal divergence (Chelton et al., 2001). Thus, warm SST anomalies increase the wind stress, and cold SST anomalies decrease the wind stress. The wind stress and wave-induced SSTs are therefore positively correlated (figures not shown). The wave pattern is clear in the regressed SSTs with a pronounced magnitude north of the Equator. The warm SSTs accompany a southeasterly wind stress, and cold SSTs accompany a northwesterly wind stress. As a result, wind stress divergence west of the cold SST anomalies and convergence to their east are induced. South of the Equator, the regressed SSTs and wind stress coefficients have a wave pattern similar to that north of the Equator, although the SST magnitude is weak.

Furthermore, when the instability waves propagate westward, the wind stress divergence and convergence spread westward almost simultaneously (Fig. 11), suggesting a wind stress adjustment to SST changes (Xie

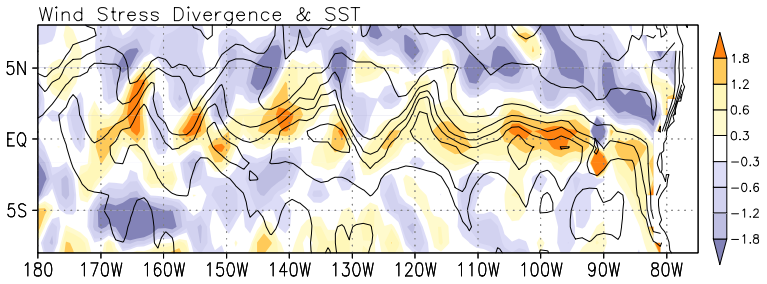

Fig. 10. A simulated 3-day mean (12–14 October, model year 0018) SST distribution (contours with 1 K interval) and wind stress divergence (shaded, 10^{-7} N m^{-3}).

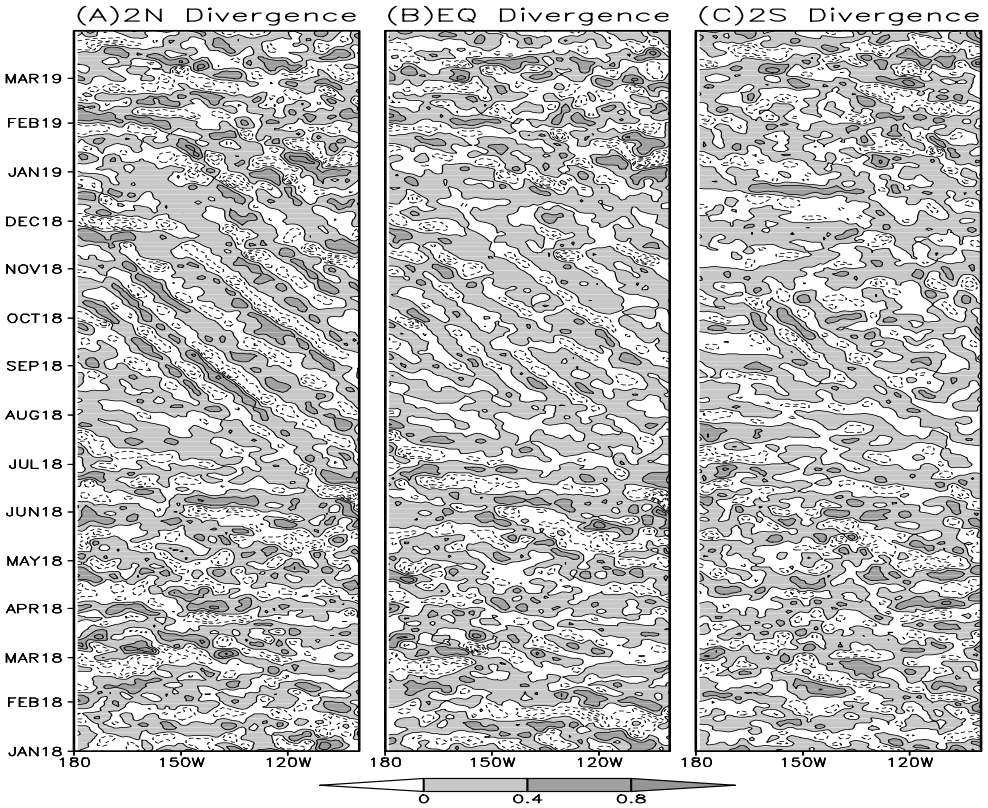

Fig. 11. Time-longitude sections of the 10- to 50-day bandpass-filtered wind divergence along (a) 2°N, (b) the Equator, and (c) 2°S. Units: 10^{-7} N m^{-3}).

et al., 1998; Liu et al., 2000; Hashizume et al., 2001). Figure 11 shows the 10- to 50-day bandpass-filtered wind stress divergence as a function of longitude and time at 2°N, the Equator, and 2°S, respectively. The influence of instability waves on wind stress is obvious in Fig. 11. The model simulation shows that a similar wind stress adjustment also occurs to the south of the Equator. However, the influence of TIWs on wind stress south of the Equator is visible only from September to November, when the surface instability waves south of the Equator are clearly discernible.

As the SST and wind stress perturbations propagate westward synchronously, the convergence (divergence) of wind stress to the west of the warm (cold) SST anomalies causes a decrease (increase) in the wind speed anomalies above. Decreasing (increasing) surface wind speed reduces (enhances) turbulent mixing and the surface latent heat of evaporation. In response to the decreased (increased) turbulent mixing and the latent evaporation, SST cooling decelerates (accelerates). Less (more) SST cooling thus leads to an increase (decrease) in SSTs to the west of warm (cold) SST anomalies. Therefore, the local air-sea interactions through the latent heat of evaporation and tur-

bulent fluxes in the equatorial Pacific favor the westward propagation of TIWs; that is, air-sea coupling appears to be a vital element of the simulated TIWs.

7. Summary and discussion

Duing et al. (1975) and Legeckis (1977) discovered the existence of TIWs in the tropical Atlantic and Pacific Oceans about 40 years ago. Satellite imagery has helped to reveal that the TIWs propagate westward in boreal summer and fall, with typical wavelengths of 1000–2000 km, phase speeds of 0.4–0.6 m s^{-1}, and periods of about 20–40 days. Although consensus on the wave-generation mechanism has not yet been reached, they have attracted much scientific attention due to their potential importance to the tropical climate. Because of the sparseness, shortness, and discontinuity of in situ observations, observational efforts have not yet yielded conclusive evidence that can fully clarify the role of TIWs in the tropical climate. In this study, typical features of TIWs were successfully reproduced by a high-resolution AOGCM, MIROC 3.2. Thus, numerical modeling, carefully validated against observations, may provide us with a valuable tool to study the energy source of TIWs and enable us to understand the contributions of TIWs to the equatorial climate.

The instability waves are clearly discernible by SST variation within a narrow band between 4°N and 4°S in the eastern tropical Pacific as observed by satellites (Chelton et al., 2001; see their Fig. 4a). However, the vertical structure of the simulation results shows that the ocean temperature fluctuations caused by TIWs have a much broader latitudinal extension in the sub-surface layer. The model simulation indicates that TIWs near the ocean surface extract barotropic energy conversion from the shear between major ocean currents, for example, the shear between the westward-flowing SEC and eastward-flowing EUC near the Equator, and the shear between the eastward-flowing NECC and westward-flowing SEC near the northern equatorial temperature front. Though barotropic energy conversion is responsible for providing the main energy source for TIWs generation, it is mostly confined to near the surface and the Equator, and does not account for the fluctuations in temperature and currents in the sub-surface layer. This deeper and northward-extended wave activity appears to gain its energy through baroclinic conversion via buoyancy work, which further contributes to the asymmetric distribution of TIWs.

Consistent with the observations, model simulations also show that TIWs quantitatively affect the equatorial oceanic heat budget. The contribution of the convergence of the meridional eddy heat flux during the wave season could offset about 30%–40% of the cooling effect caused by the climatological equatorial upwelling of the mean flows in the equatorial Pacific (Fig. 10). Observational estimates are consistent with the warming contribution of the eddy heat flux to the tropical ocean heat budget, but have a wider range; for example, Hansen and Paul (1984) thought that the contribution could be as high as approximately 66%. Observations also found that TIWs were affected by ENSO; they were fully developed in the cold phase of ENSO and suppressed during the warm phase (Contreras, 2002; Yu and Liu, 2003). Therefore, An (2008) has suggested that the meridional thermal flux of TIWs in the ocean mixed layer is negatively correlated with the tropical eastern Pacific SST anomalies, which may suggest a negative feedback to ENSO development.

The present results regarding the contribution of TIWs to the mixed layer heat budget of the tropical Pacific ocean are encouraging, since most current OGCMs and coupled AOGCMs tend to produce a cold bias in the cold tongue simulation; that is, the cold tongue is too strong and extends too far west compared to the observations. In terms of the importance of air-sea interactions in establishing tropical Pacific climatology, efforts to reduce the cold-tongue bias in OGCMs and AOGCMs, including improvement of the parameterization schemes, have been made. TIWs warm the tropical ocean by transporting heat to the Equator and therefore reduce the strength of the cold tongue. On the other hand, given the possibility of negative feedback of TIWs to ENSO development, further study may provide more information on ENSO climate variability.

The correlations between the SST fluctuations associated with TIWs and the variation of air temperature and wind velocity just above the ocean are positive. Moreover, the SST gradient induced by TIWs as the instability waves propagate westward during the wave season causes a boundary layer adjustment with wind stress divergence over the cusp-shaped SST front just north of the Equator. This is thought to be the consequence of a change in the vertical mixing of air (Wallace et al., 1989; Hayes et al., 1989). As the low-level air crosses the cold tongue SSTs to the northern warm SSTs, the atmospheric boundary layer is destabilized over the warmer water, resulting in enhanced turbulent mixing and increased wind stress. Thus, a divergence of the surface wind stress over the north side of the cold tongue with the strongest latitudinal SST gradient in the eastern tropical Pacific is induced (Fig. 10). As assumed by the vertical mixing mechanism, when the low-level air crosses from the southern warm surface waters to the cold tongue, the decreased

SSTs stabilize the air and reduce the wind stress; convergence of the surface wind is therefore induced. This resultant convergence is shown in Fig. 10. Given that the perturbation of wind stress is associated with the SST gradient, the divergence and convergence of wind stress accompanied by TIW-induced SST fluctuations are of the same magnitude and propagate westward with SST fluctuations (see Fig. 11).

The atmospheric response to TIW-induced SST fluctuations positively feeds back to the TIWs. As the SST and wind stress perturbations propagate westward synchronously, the convergence of wind stress is west of the warm SST anomalies, and the consequent decrease in wind speed reduces the turbulent mixing and latent evaporation. Thus, this causes an increase in SST west of the warm SST anomalies, favoring the westward propagation of TIWs.

Simulations of tropical instability waves (TIWs) by a relatively high-resolution coupled atmosphere-ocean model have been described and a positive impact on the cold tongue climate has been suggested. Impacts on ENSO variability and other aspects of climate need to be clarified by further studies. Simulations of TIWs require high resolution, both in the ocean and in the atmosphere, and are computationally costly. However, higher resolution climate models should promote our understanding of the climate system and its workings, not just in the equatorial oceans but in other parts of the globe as well.

Acknowledgements. The authors would like to thank Drs. Suzuki and Yang for their help in handling the data. The first author was supported by the Postdoctoral Fellowship given by the Japan Society for the Promotion of Science. This work was also supported by the Kyousei and Kakushin Projects of the ministry of Education, Culture, Sports, Science, and Technology of Japan, the Core Research for Evolutional Science and Technology of the Japan Science and Technology Agency, and the National Basic Research Program of China (Grant No. 2006CB403606).

REFERENCES

An, S.-I., 2008: Interannual variations of the tropical ocean instability wave and ENSO. *J. Climate*, **21**, 3680–3686.

Arakawa, A., and W. H. Schubert, 1974: Interactions of cumulus cloud ensemble with the large-scale environment. Part I. *J. Atmos. Sci.*, **31**, 671–701.

Chelton, D. B., F. J. Wentz, C. L. Gentemann, R. A. de Szoeke, and M. G. Schilax, 2000: Satellite microwave SST observations of transequatorial tropical instability waves. *Geophys. Res. Lett.*, **27**, 1239–1242.

Chelton, D. B., and Coauthors, 2001: Observations of coupling between surface wind stress and sea surface temperature in the eastern tropical Pacific. *J. Climate*, **14**, 1479–1298.

Contreras, R. F., 2002: Long-term observations of tropical instability waves. *J. Phys. Oceanogr.*, 32, 2715–2722.

Cox, M., 1980: Generation and propagation of 30-day waves in a numerical model of the Pacific. *J. Phys. Oceanogr.*, **10**, 1168–1186.

Duing, D., and Coauthors, 1975: Meanders and long waves in the equatorial Atlantic. *Nature*, **257**, 280–284.

Flament, P., S. Kennan, R. Knox, P. Niiler, and R. Bernstein, 1996: The three-dimensional structure of an upper ocean vortex in the tropical Pacific. *Nature*, **383**, 610–613.

Hansen, D. V., and C. A. Paul, 1984: Genesis and effects of long waves in the equatorial Pacific. *J. Geophys. Res.*, **89**, 10431–10440.

Hashizume, H., S.-P. Xie, W. T. Liu, and K. Takeuchi, 2001: Local and remote response to tropical instability waves: A global view from space. *J. Geophys. Res.*, **106**, 10173–10185.

Hashizume, H., S.-P. Xie, M. Fujiwara, M. Shiotani, T. Watanabe, Y. Tanimoto, W. T. Liu, and K. Takeuchi, 2002: Direct observations of atmospheric boundary layer response to slow SST variations on the Pacific equatorial front. *J. Climate*, **15**, 3379–3393.

Hasumi, H., 2000: CCSR ocean component model (COCO) version 2.1, CCSR, Rep. 13, 68pp.

Hasumi, H. and S. Emori, 2004: K-1 coupled model (MIROC) description,, K-1 Tech. Rept. 1. Center for Climate System Research, University of Tokyo, Kashiwa, Japan, 34pp.

Hayes, S. P., M. J. McPhaden, and J. M. Wallace, 1989: The influence of sea surface temperature on surface wind in the eastern equatorial Pacific. *J. Climate*, **2**, 1500–1506.

Jochum, M., M.-R. Paola, and B. Antonio, 2004: Tropical instability waves in the Atlantic Ocean. *Ocean Modelling*, **7**, 145–163.

Legeckis, R., 1977: Long waves in the eastern equatorial Pacific Ocean: A view from a geostationary satellite. *Science*, **197**, 1179–1181.

Liu, W. T., X. Xie, P. S. Polito, S.-P, Xie, and H. Hashizume, 2000: Atmospheric manifestation of tropical instability waves observed by QuickSCAT and Tropical Rain Measuring Mission. *Geophys. Res. Lett.*, **27**, 2545–2548.

Luther, D. S., and E. S. Johnson, 1990: Eddy energetics in the upper equatorial Pacific during the Hawaii-to-Tahiti Shuttle Experiment. *J. Phys. Oceanogr.*, **20**, 913–944.

Lyman, J. M., G. C. Johnson, and W. S. Kessler, 2007: Distinct 17-day and 33-day Tropical Instability Waves in subsurface temperature observations. *J. Phys. Oceanogr.*, **37**, 855–872.

Masina, S., and S. Philander, 1999: An analysis of tropical instability waves in a numerical model of the Pa-

cific Ocean—1. Spatial variability of the waves. *J. Geophys. Res.*, **104**, 29613–29635.

Masina, S., S. Philander, and A. Bush, 1999: An analysis of tropical instability waves in a numerical model of the Pacific Ocean—2. Generation and energetics of the waves. *J. Geophys. Res.*, **104**, 29613–29635.

McCreary, J. P., and Z. Yu, 1992: Equatorial dynamics in a 2 1/2-layer model. *Progres in Oceanography*, **29**, 152–176.

McPhaden, M. J., and Coauthors, 1998: The Tropical Ocean-Global Atmosphere observing system: A decade of progress. *J. Geophys. Res.*, **103**, 14169–14240.

Mellor, G. L., and T. Yamada, 1982: Development of a turbulence closure model for geostrophic fluid problems. *Rev. Geophys.*, **20**, 851–875.

Nakajima, T., M. Tsukamoto, Y. Tsushima, A. Numaguti, and T. Kimura, 2000: Modelling of the radiative process in an atmospheric general circulation model. *Appl. Opt.*, **39**, 4869–4878.

Noh, Y., and H.-J. Kim, 1999: Simulations of temperature and turbulence structure of the oceanic boundary layer with the improved near-surface process. *J. Geophys. Res.*, **104**, 15621–15634.

Numaguti, A., M. Takahashi, T. Nakajima, and A. Sumi, 1997: Description of CCSR/NIES atmospheric general circulation model. CGER's supercomputer monograph report, Center for Global Environmental Research, National Institute for Environmental Studies, No. 3, 1–48.

Pan, D.-M., and D. A. Randall, 1998: A cumulus parameterization with a prognostic closure. *Quart. J. Roy. Meteor. Soc.*, 124, 949–981.

Philander, S. G. H., 1976: Instabilities of zonal equatorial currents. *J. Geophys. Res.*, **81**, 3725–3735.

Philander, S. G. H., 1978: Instabilities of zonal equatorial currents, 2. *J. Geophys. Res.*, **83**, 3679–3682.

Proehl, J. A., 1996: Linear stability of equatorial flows. *J. Phys. Oceanogr.*, **26**, 601–621.

Qiao, L., and R. H. Weisberg, 1998: Tropical instability wave energetics: Observations from the Tropical Instability Wave Experiment. *J. Phys. Oceanogr.*, **28**, 345–360.

Semtner, A. J., and W. R. Holland, 1980: Numerical simulation of equatorial ocean circulation, 1, A basic case in turbulent equilibrium. *J. Phys. Oceanogr.*, **10**, 667–693.

Small, R. J., S.-P. Xie, and Y. Wang, 2003: Numerical simulation of atmospheric response to Pacific tropical instability waves. *J. Climate*, **16**, 3723–3741.

Swenson, M. S., and D. V. Hansen, 1999: Tropical Pacific Ocean mixed layer heat budget: The Pacific cold tongue. *J. Phys. Oceanogr.*, **29**, 69–81.

Vialard, J., C. Menkes, D. L. T. Anderson, and M. A. Balmaseda, 2003: Sensitivity of Pacific Ocean tropical instability waves to initial conditions. *J. Phys. Oceanogr.*, **33**, 105–121.

Wallace, J. M., T. P. Mitchell, and C. Deser, 1989: The influence of sea surface temperature on surface wind in the eastern equatorial Pacific: Seasonal and interannual variability. *J. Climate*, **2**, 1492–1499.

Weisberg, R. H., and T. J. Weingartner, 1988: Instability waves in the equatorial Atlantic Ocean. *J. Phys. Oceanogr.*, **18**, 1641–1657.

Xie, S. P., M. Ishiwatari, H. Hashizume, and K. Takeuchi, 1998: Coupled ocean-atmospheric waves on the equatorial front. *Geophys. Res. Lett.*, **25**, 2185–2188.

Yu, Z., J. P. McCreary, and J. A. Proehl, 1995: Meridional asymmetry and energetics of tropical instability waves. *J. Phys. Oceanogr.*, **25**, 2997–3007.

Yu, J., and W. T. Liu, 2003: A linear relationship between ENSO intensity and tropical instability wave activity in the eastern Pacific Ocean. *Geophys. Res. Lett.*, **30**, 1735.